

Early Planet Formation in Embedded Disks (eDisk). XVIII. Indication of a Possible Spiral Structure in the Dust Continuum Emission of the Protostellar Disk around IRAS 16544-1604 in CB 68

Sanemichi Z. TAKAHASHI,^{1,2,†} Shigehisa TAKAKUWA,^{1,3} Ryosuke NAKANISHI,⁴ Yusuke TSUKAMOTO,¹ Kazuya SAIGO,^{1,2} Miyu KIDO,^{1,3} Nagayoshi OHASHI,³ Zhi-Yun LI,⁵ Leslie W. LOONEY,⁶ Zhe-Yu Daniel LIN,⁵ Mayank NARANG,³ Kengo TOMIDA,⁷ John J. TOBIN,⁸ Jes K. Jørgensen⁹

¹Department of Physics and Astronomy, Graduate School of Science and Engineering, Kagoshima University, 1-21-35 Korimoto, Kagoshima, Kagoshima 890-0065, Japan 181-8588, Japan

²National Astronomical Observatory of Japan, 2-21-1 Osawa, Mitaka, Tokyo 181-8588, Japan

³Academia Sinica Institute of Astronomy & Astrophysics, 11F of Astronomy-Mathematics Building, AS/NTU, No.1, Sec. 4, Roosevelt Rd, Taipei 10617, Taiwan

⁴Physics and Astronomy Program, School of Science, Kagoshima University, 1-21-35 Korimoto, Kagoshima, Kagoshima 890-0065, Japan 181-8588, Japan

⁵University of Virginia, 530 McCormick Rd., Charlottesville, Virginia 22904, USA

⁶Department of Astronomy, University of Illinois, 1002 West Green St, Urbana, IL 61801, USA

⁷Astronomical Institute, Graduate School of Science, Tohoku University, Sendai 980-8578, Japan

⁸National Radio Astronomy Observatory, 520 Edgemont Rd., Charlottesville, VA 22903 USA

⁹Niels Bohr Institute, University of Copenhagen, Øster Voldgade 5-7, 1350, Copenhagen K, Denmark

*E-mail: sanemichi.takahashi@gmail.com, takakuwa@sci.kagoshima-u.ac.jp, tsukamoto.yusuke@sci.kagoshima-u.ac.jp, saigokz@gmail.com, k1530218@kadai.jp, ohashi@asiaa.sinica.edu.tw, zl4h@virginia.edu, lwl@illinois.edu, zdl3gk@virginia.edu, mayankn1154@gmail.com, tomida@astr.tohoku.ac.jp, jtobin@nrao.edu, jesk.jorgensen@gmail.com

ORCID: 0000-0003-3038-364X, 0000-0003-0845-128X, 0000-0001-6738-676X, 0000-0003-1549-6435, 0000-0002-2902-4239, 0000-0003-0998-5064, 0000-0002-7402-6487, 0000-0002-4540-6587, 0000-0001-7233-4171, 0000-0002-0554-1151, 0000-0001-8105-8113, 0000-0002-6195-0152, 0000-0001-9133-8047

Abstract

We performed numerical simulations along with radiative transfer calculations to reproduce an intriguing asymmetric shoulder feature in the dust continuum emission of the protostellar disk around one of the eDisk targets, Class 0 protostar IRAS 16544-1604 in CB 68. This is our first attempt to bridge between theoretical works of protostellar disk evolution and the eDisk observations. We found that while our hydrodynamic simulations form spiral structures caused by gravitational instability, they become less discernible after the disk is inclined and convolved with the telescope beam. The widths of the spiral structure as obtained by our numerical simulations are $\sim 0.1 - 0.8$ times the eDisk beam size of 4.5 au. Our modeling effort implies that the apparent absence of spiral features in the eDisk observations does not necessarily indicate the real absence of internal substructures and gravitational instability. We also found that the asymmetric shoulder structure of the continuum profile along the major axis appears when the disk is massive enough with a Toomre parameter $Q \sim 1$. This mechanism offers a potential explanation for the observed, asymmetric shoulder features in the disks surrounding IRAS 16544-1604 and the other eDisk sources.

Keywords: radiative transfer, methods: numerical, stars: protostars

1 Introduction

Protoplanetary disks are the birthplaces of planets. Since the physical conditions of protoplanetary disks profoundly influence the planet formation processes (Boss 1997; Kornet et al. 2005; Mordasini et al. 2012; Mulders et al. 2015a, 2015b; Narang et al. 2018), a comprehensive understanding of the disk properties is crucial for developing planet formation theories. High resolution observations of protoplanetary disks in Class II sources reveal that the dust continuum emission in the disks is not smooth but shows intriguing structures, such as spiral arms (*e.g.*, Pérez

et al. 2016), crescents (*e.g.*, van der Marel et al. 2013; Fukagawa et al. 2013), and ring-gap structures (*e.g.*, ALMA Partnership et al. 2015; Andrews et al. 2016; Isella et al. 2016; Sheehan & Eisner 2017; Fedele et al. 2017, 2018). Especially, Disk Substructures at High Angular Resolution Project (DSHARP) (Andrews et al. 2018) observations have found that ring-gap structures are common in protoplanetary disks, which are considered to be carved by the hidden protoplanets. On the contrary, our ALMA Large Program, "Early Planet Formation in Embedded Disks (eDisk)", has found that majority of protostellar disks around Class 0 / I sources do not exhibit such ring-gap features, except for the disks around the most evolved Class I sources of L1489 IRS (Sai et al.

[†] Present address: Matsuda Company

2023) and Oph IRS 63 (Flores et al. 2023). Instead, in many of the eDisk sources (L1527 IRS, IRAS 16253-2429, GSS 30 IRS3, IRAS 16544-1604, R CrA IRAS 32B, IRAS 04302+2247, and R CrA IRS7B-a), the 1.3-mm dust images exhibit asymmetric intensity profiles along the disk minor axes. Our radiative transfer modeling has revealed that the asymmetric intensity profiles along the disk minor axes can be interpreted as the effect of the dust flaring and optically-thick dust emission (Ohashi et al. 2023; Takakuwa et al. 2024).

Several eDisk sources also exhibit intriguing shoulder, bump, or asymmetric features along the disk major axes. In L1527 IRS, a Class 0 protostar in Taurus, the southern part of the north-south elongated disk feature is stronger and wider along the transverse direction than the northern part (Sheehan et al. 2022; van't Hoff et al. 2023). Toward Ced110 IRS4A, a Class 0 source in the Chamaeleon I region, bump features are clearly seen at radii of 30-70 au, with a slight asymmetry along the major axis. Three intensity peaks to the west, center, and east are seen along the disk major axis toward Ced110 IRS4B, where the western peak is slightly stronger than the eastern peak (Sai et al. 2023). A Class 0 source of IRAS 16253-2429 in Ophiuchus clearly exhibits an asymmetric intensity profile along the disk major axis (Aso et al. 2023). Toward the Class 0 protostar R CrA IRS5N (Sharma et al. 2023) and Class I protostar R CrA IRS 7B-a (Takakuwa et al. 2024), the locations of the emission peaks are shifted from the geometrical disk center along the major axes. Double-side, shoulder features are identified in the protostellar disk of GSS 30 IRS 3 at radii of 25 and 50 au (Santamaría-Miranda et al. 2024), while an one-side shoulder is seen toward IRAS 16544-1604 at a radius of ~ 15 au (Kido et al. 2023), both of which are Class 0 sources in Ophiuchus. These results imply that protostellar disks have internal, possibly non-axisymmetric, substructures. The nature of such internal structures is, however, yet to be elucidated.

According to numerical simulations of star and disk formation, young protostellar disks can be massive enough to be gravitationally unstable (*e.g.*, Bate 1998; Inutsuka et al. 2010). In such a gravitationally unstable disk, spiral arms should be formed, which play an important role in angular momentum transfer (*e.g.*, Machida et al. 2011; Tsukamoto et al. 2015a). Absence of such spiral features implies that these disks are gravitationally stable, unless such features appear only in a short time scale for observations. The source of the bump or shoulder features observed by eDisk could be such spiral structures hidden in the protostellar disks. To investigate the origin and physics of the observed bump / shoulder features, hydrodynamic simulations coupled with radiative transfer calculations are essential.

This paper is the first such attempt to compare results of hydrodynamical simulations plus radiative transfer calculations to the eDisk images. Such a comparison requires a number of model parameters and their fine tuning, and it is impractical to conduct such a task for all the eDisk images at once. We focus on disk structures around IRAS 16544-1604 (hereafter IRAS 16544), which exhibits a clear shoulder feature along the disk major axis. This object is located in the southwestern outskirts of the Ophiuchus North region at a distance of 151 pc (Zucker et al. 2020), and its bolometric luminosity and central protostellar mass are estimated to be $0.89 L_{\odot}$ (Ohashi et al. 2023) and $0.14 M_{\odot}$ (Kido et al. 2023)¹, respectively. Figure 1 shows the 1.3 mm dust continuum image of the protostellar disk in IRAS 16544 taken from Kido et al. (2023). The observed dust disk radius, which is determined by the region where

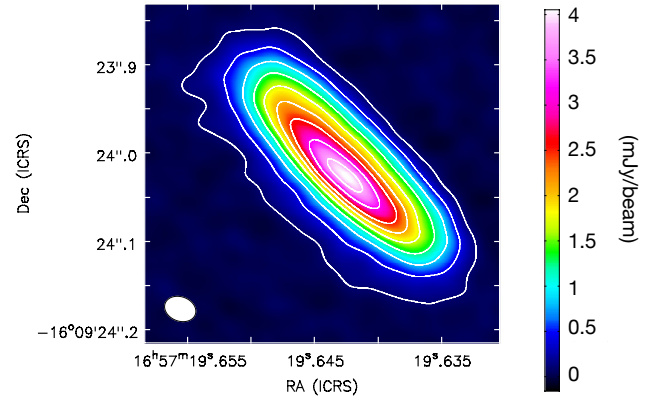


Fig. 1: 1.3 mm dust continuum image in IRAS 16544 obtained by eDisk (Kido et al. 2023). Contour levels are 5σ , 20σ , 40σ , 60σ , 80σ , 100σ , 120σ , and 180σ ($1\sigma = 21 \mu\text{Jy beam}^{-1}$). The beam size is $0''.036 \times 0''.027$ (P.A. = 69 degree), as shown in a filled ellipse at the bottom-left corner. Alt text: Color and contour image.

the dust continuum intensity exceeds 5σ ($1\sigma = 21 \mu\text{Jy beam}^{-1}$), is ~ 30 au. While there is no clear spiral structure seen in the image, the brightness temperature profile along the disk major axis shows an asymmetry with a “shoulder” structure (Figure 2)². Kido et al. (2023) estimated the total gas + dust disk mass in the range from $1.63 \times 10^{-3} M_{\odot}$ to $1.02 \times 10^{-2} M_{\odot}$ for the assumed dust temperature of 20 - 100 K. These estimates should be regarded as the lower limit of the disk mass because of the assumption of the optically thin dust emission. This gives the upper limit of the Toomre Q value of 2.7 - 17. Therefore, it is possible that the disk is gravitationally unstable.

We calculated density and temperature distributions of gravitationally unstable disks by numerical simulations and evaluated the intensity distributions of the 1.3 mm continuum emission arising from the disks using radiative transfer calculations. Through the comparison between the intensity profiles obtained from theoretical calculations and the observations, we investigated the disk substructure that can explain the observations, specifically, the asymmetric shoulder structure observed by eDisk. Although the comparison between the spiral structures observed around Elias 2–27 (Pérez et al. 2016) and produced by numerical simulations of the gravitationally unstable disk has already been presented in Tomida et al. (2017), the detectability of the spiral arms is not well studied so far. We also discuss the requirement to observationally detect the spiral arms in the protostellar disk based on the physical values obtained from the numerical simulations.

This paper is organized as follows. In Section 2, the setup of the numerical simulations of the self-gravitating disk and the radiative transfer calculations is presented. Section 3 shows the results of the numerical simulations and the radiative transfer calculations. Sections 4 and 5 provide a few key insights obtained from our work and conclusions, respectively.

² The origin and the major axis for the profile are determined by the 2-dimensional Gaussian fitting to the observed 1.3-mm image. Through the radiative transfer calculations, we have verified that the simple 2-dimensional Gaussian fitting is sufficient to derive the central protostellar position and the major axis, even if the 3-dimensional disk structure has a flared geometry (see Appendix A).

¹ This dynamical mass is obtained from the fitting of the C^{18}O (2–1) ridge emission in the Position - Velocity diagram.

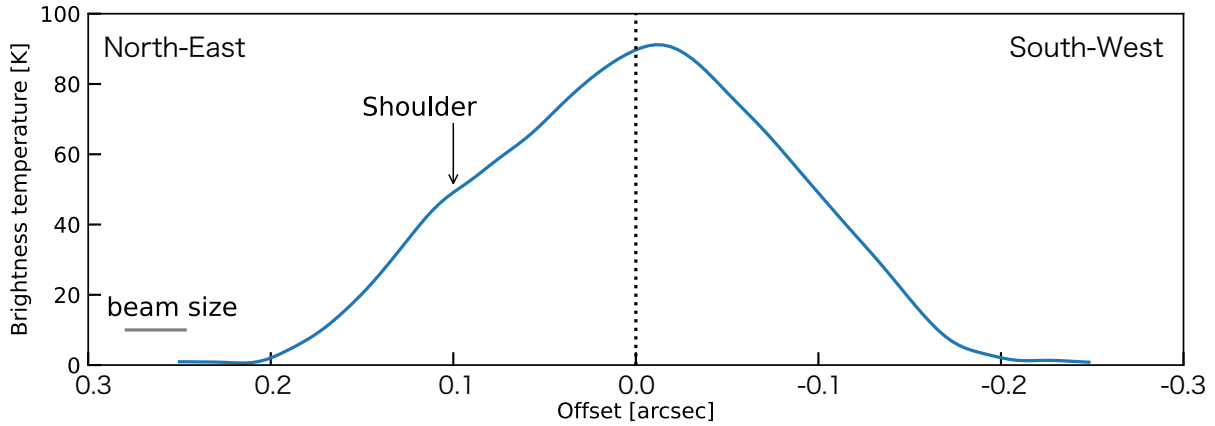


Fig. 2: Observed brightness temperature profile of the 1.3 mm dust continuum emission along the disk major axis in IRAS 16544. The beam size is shown in the bottom left. A shoulder structure is observed in the left-hand side of this profile. Alt text: Line graph. x axis shows the positional offset from the protostellar position from 0.3 to -0.3 arcsecond. The y axis shows the brightness temperature in Kelvin.

2 Method

2.1 Basic Equations of Numerical Simulation

A grid-based two-dimensional hydrodynamical simulation code, FARGO-ADSG, is adopted to calculate the disk gas dynamics and spiral structure formation through the gravitational instability. The equations solved in the simulation are as follows:

$$\frac{\partial \Sigma}{\partial t} + \nabla \cdot (\Sigma \mathbf{v}) = 0 \quad (1)$$

$$\Sigma \left(\frac{\partial \mathbf{v}}{\partial t} + \mathbf{v} \cdot \nabla \mathbf{v} \right) = -\nabla P - \nabla \Phi \quad (2)$$

$$\frac{\partial E}{\partial t} + \nabla (E \mathbf{v}) = -P \nabla \cdot \mathbf{v} - \Lambda_c, \quad (3)$$

where Σ is the gas surface density, \mathbf{v} is the gas velocity, E is the gas internal energy per unit area, P is the vertically integrated pressure, Φ is the gravitational potential, and Λ_c is the net cooling rate per unit area. Although the heating term is not included in this equation explicitly, the effects of the radiation and accretion heating are included in the net cooling rate (see the explanation of Equation 6 below). P is calculated assuming an ideal gas equation of state with the thin disk approximation,

$$P = (\gamma - 1)E, \quad (4)$$

where $\gamma = 5/3$ is the ratio of specific heat. Gas and dust are assumed to be at the same temperature and the temperature T is calculated from

$$T = \frac{\mu m_H}{k_B} \frac{P}{\Sigma}, \quad (5)$$

where $\mu (= 2.34)$, m_H , and k_B are the mean molecular weight, the hydrogen mass, and the Boltzmann constant, respectively.

The viscous term is not included in the equation of motion (Equation 2), as viscosity does not play an important role in spiral structure formation. Spiral arms due to gravitational instability form and disperse recurrently within the dynamical timescale. In contrast, the viscous timescale is much longer than the dynamical timescale. When the width of the spiral is similar to the pressure scale height (see Section 4.1), the viscous timescale can be estimated as $\sim 1/(\alpha\Omega)$, where α is the parameter representing the strength of viscosity and Ω is the Keplerian frequency. For example, at a radius of 30 au, the dynamical time is $\sim 1/\Omega = 70$ yr and the viscous time is $\sim 1/(\alpha\Omega) = 7000$ yr on the assumption of

$\alpha = 0.01$. In cases where α is much smaller than unity, viscosity can be considered negligible.

The net cooling rate Λ_c is given as follows (Hubeny 1990),

$$\Lambda_c = \frac{8}{3} \sigma (T^4 - T_{\text{eq}}^4) \frac{\tau}{\frac{1}{4}\tau^2 + \frac{1}{\sqrt{3}}\tau + \frac{2}{3}}, \quad (6)$$

where σ is the Stefan-Boltzmann constant, T_{eq} is the equilibrium temperature, and τ is the optical depth of the dust continuum emission. As will be shown below the 1.3-mm dust-continuum emission is optically thick. The distribution of the equilibrium temperature ($\equiv T_{\text{eq}}$) in the disk is set to roughly reproduce the observed 1.3-mm brightness temperature distribution without the shoulder structure as,

$$T_{\text{eq}} = \max[T_{\text{peak}} - Ar, 10[\text{K}]], \quad (7)$$

where r is the radius from the central star, $T_{\text{peak}} = 100$ K is the peak temperature of the disk consistent with the observed peak brightness temperature of the 1.3-mm dust-continuum emission, and $A = 3$ (K au^{-1}) is the temperature gradient of the disk estimated from the observations³ (Kido et al. 2023). The optical depth $\tau = \kappa_R \Sigma$ is obtained using the Rosseland mean opacity per unit gas mass ($= \kappa_R$) calculated from the opacity model given by Birnstiel et al. (2018) with the minimum and maximum dust sizes⁴ of 0.1 μm and 1 mm and a power-law index of the grain size distribution of -3.5. The dust is assumed to be dynamically and thermally coupled with gas, and the gas-to-dust mass ratio to be 100. If compressional heating is ineffective in the disk (when the first term on the right-hand side of Equation 3 is negligible), the disk temperature evolves so that the cooling rate Λ_c is zero, *i.e.*, $T = T_{\text{eq}}$. Λ_c represents the radiative cooling in the vertical direction of the disk when $T_{\text{eq}} = 0$. Non-zero T_{eq} corresponds to the addition of a heating term. Since the temperature distribution of the disk is

³ If a power law distribution of T_{eq} is adopted as commonly used in the disk temperature distribution, the temperature around the central region becomes significantly higher than the observed brightness temperature. Therefore, for comparison with observations, we use the observed brightness temperature to model T_{eq} . If the temperature structure in the z -direction is calculated directly, the temperature distribution at the $\tau \sim 1$ surface may closely match the observed brightness temperature, even with a power law temperature distribution in the midplane. However, since this 2-dimensional study cannot handle the temperature structure in the z -direction, we adopt this approximate method.

⁴ Since the maximum dust size in protostellar disks is still controversial, it is assumed to be 1 mm in this work. Numerical simulations have reproduced dust growth up to 1 mm in protostellar disks (Tsukamoto et al. 2023).

affected not only by the radiative cooling term but also by advection and compressional heating, the temperature distribution of the simulated disk deviates from T_{eq} .

2.2 Numerical Procedure and Initial Conditions

In the numerical simulations, the 2-dimensional polar grid (r, ϕ) is adopted. The inner and outer boundaries of the numerical simulations are set to be 1 au and 300 au, respectively, and the open boundary condition (the gradients of the physical values are assumed to be 0 at the boundaries) is used. The numerical simulations do not include the envelope component. The grid numbers for the radial and azimuthal directions are 512 and 1024, respectively. The central protostellar mass is set to be $M_* = 0.14 M_\odot$, as derived by Kido et al. (2023). The initial temperature distribution is given by $T_{\text{ini}} = T_{\text{eq}}$. The initial surface density is given as

$$\Sigma_{\text{ini}} = \Sigma_{1\text{au}} \left(\frac{r}{1 \text{ au}} \right)^{-1.3} \sqrt{\frac{T_{\text{ini}}}{97 \text{ K}}} \exp\left(-\frac{r}{r_{\text{disk}}}\right), \quad (8)$$

where $\Sigma_{1\text{au}}$ is the surface density at $r = 1$ au, and $r_{\text{disk}} (\gg 1 \text{ au})$ is the outer disk radius determined by the exponential taper. The radial exponent -1.3 and the $\sqrt{T_{\text{ini}}}$ term are adopted to keep the Toomre's Q values (Toomre 1964) approximately constant in the inner region of the disk. This initial surface density profile is expected from hydrodynamic simulations of disk formation (Tsukamoto et al. 2015b). The term $\sqrt{T_{\text{ini}}/97 \text{ K}}$ cancels the dependence of Q values on the sound speed, where 97 K is the initial temperature at $r = 1$ au.

A small level (=0.1 per cent) of white noise is added to the initial surface density as an initial perturbation of the gravitational instability. The initial radial velocity is zero, and the initial azimuthal velocity is provided to balance the centrifugal and pressure gradient force with the gravitational force. Three models (Models 1, 2, and 3) with different initial disk surface densities and thus disk masses are adopted. The adopted values of $\Sigma_{1\text{au}}$ and disk masses are listed in Table 1. The disk mass of Model 1 is smaller than the central protostellar mass, that of Model 2 is comparable to the protostellar mass, and that of Model 3 is higher than the protostellar mass. These three models yield the initial value of $Q = c_s \Omega / (\pi G \Sigma)$ of ~ 2 , 1.3, and 1.0, respectively (Figure 3), where c_s is the sound speed and Ω is the angular velocity. The disk outer radius is set as $r_{\text{disk}} = 60$ au, which is the outermost radius where the Keplerian rotation is observed in the C^{18}O (2–1) emission (Kido et al. 2023). Parameters used for the disk models are summarized in Table 1.

With these initial conditions, evolutions of the surface density and (vertically-averaged) temperatures are calculated through numerical simulations. For Models 1 and 2, numerical simulations are continued until $t = 2.4 \times 10^4$ yr. This duration is long enough for the growth of spiral arms due to the gravitational instability. For Model 3, the speed of the numerical simulation becomes much slower than the other two models, due to the higher disk surface density and gravitational instability. The results of Model 3 at $t = 3.5 \times 10^3$ yr are presented, which corresponds to the 8 orbital period at $r = 30$ au. At this time three spiral, $m = 3$ feature has been developed. On the other hand, after $t \sim 3.9 \times 10^3$ yr the model disk is fragmented to show a binary feature, which is not applicable to the present case of IRAS 16544. The surface density and temperature distributions are then input to the radiative transfer calculations with RADMC3d described below.

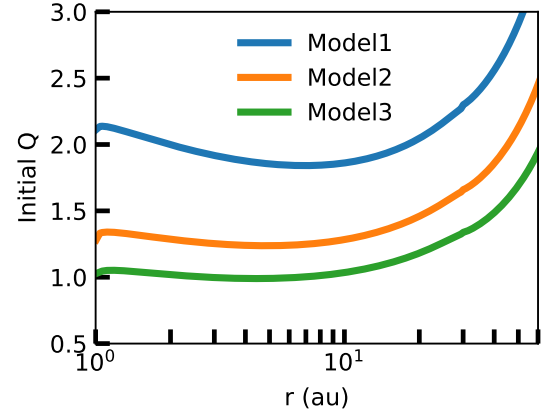


Fig. 3: Radial distribution of initial Q values for Models 1, 2 and 3. Alt text: Line graph. x axis shows the radius from 1 to 60 astronomical unit in log scale. The y axis shows the Toomre Q value from 0.5 to 3 in linear scale.

2.3 Radiation Transfer Calculations

To perform radiative transfer calculations, density and temperature distributions in the 3-dimensional space need to be constructed from the 2-dimensional hydrodynamic results with FARGO-ADSG. On the assumption of the vertically isothermal condition, the 2-dimensional temperature distribution $T(r, \phi)$ is converted into the three dimensional temperature distribution $T(r, \phi, z)$. Whereas the vertical isothermal condition is oversimplified, it is sufficient for the purpose of the present study that compares the observed and model dust-continuum images and investigates the possible source of the observed shoulder feature. The vertical gas density distribution is assumed to be Gaussian, and the formulation of the scale height H by Bertin & Lodato (1999) is adopted, which is suitable for self-gravitating massive disks,

$$H(r, \phi) = \frac{c_s^2}{\pi G \Sigma} \left(\frac{\pi}{4Q^2} \right) \left[\sqrt{1 + \frac{8Q^2}{\pi}} - 1 \right]. \quad (9)$$

The observed extent of the dust continuum emission is $r_{\text{dust}} \sim 30$ au above the 5σ level, while the gas disk radius is $r_{\text{out}} \sim 60$ au. We found that the same radius for both the dust and gas disks makes the spatial extent of the model continuum image too large compared to that of the observed image. An exponential cutoff of the dust density is thus added as

$$\rho_{\text{dust}}(r, \phi, z) = \epsilon \frac{\Sigma_{\text{gas}}(r, \phi)}{\sqrt{2\pi} H(r, \phi)} \exp\left(-\frac{r}{r_{\text{dust}}}\right) \exp\left(-\frac{1}{2} \left(\frac{z}{H(r, \phi)}\right)^2\right), \quad (10)$$

where $\Sigma_{\text{gas}}(r, \phi)$ denotes the gas surface density obtained from the FARGO-ADSG simulations, and $\epsilon = 0.01$ is the dust-to-gas mass ratio. While this is an additional, ad-hoc procedure, this manipulation does not affect results and physics of the numerical simulations of the spiral-arm formation. It is not straightforward to reproduce the different gas and dust radii with numerical simulations. A smaller dust radius than the gas radius has also been found in another eDisk target, R CrA IRS7B-a (Takakuwa et al. 2024).

With the 3-dimensional density and temperature distributions given above, radiative transfer calculations using RADMC-3D (Dullemond et al. 2012) are performed. The disk inclination angle

Table 1: Summary of the model parameters

Model parameters adopted from Kido et al. (2023)		
Central protostellar mass	M_*	$0.14 M_\odot$
Peak temperature	T_{peak}	100 [K]
Temperature gradient	A	3 [K au $^{-1}$]
Disk outer radius	r_{out}	60 [au]
Dust disk radius	r_{dust}	30 [au]
Beam size for Gaussian convolution		4.5 au
The other parameters		
Surface density at 1 au	$\Sigma_{1\text{au}}$	1.2×10^4 [g cm $^{-2}$] (Model 1)
		2.1×10^4 [g cm $^{-2}$] (Model 2)
		2.5×10^4 [g cm $^{-2}$] (Model 3)
Initial disk gas mass		0.1 M_\odot (Model 1)
		0.17 M_\odot (Model 2)
		0.21 M_\odot (Model 3)
Radial exponent of the surface density profile		-1.3
Dust-to-gas mass ratio	ϵ	0.01
Opacity at 1.3 mm	$\kappa_{1.3\text{mm}}$	1.88 cm 2 g $^{-1}$

is set to be 73° as obtained from the observations. The wavelength of the radiation transfer is 1.3 mm for the comparison with the eDisk observations. The dust model used to calculate the opacity at 1.3 mm is based on the model of the DSHARP collaboration (Birnstiel et al. 2018), which assumes a dust size distribution with the minimum and maximum dust sizes of 0.1 μm and 1 mm, respectively, and a power-law index of -3.5. This is the same model used to calculate the Rosseland mean opacity in the hydrodynamic simulation. The resultant opacity at 1.3 mm is $\kappa_{1.3\text{mm}} = 1.88$ [cm 2 g $^{-1}$]. After the radiative transfer calculations, the resultant model images are convolved by a Gaussian with a FWHM of 4.5 au, which approximately corresponds to the beam size of the eDisk observations.

3 Results

3.1 Model 1: Low Surface Density Case

The surface density and temperature distributions of Model 1, the case of the low initial surface density, after $t = 2.4 \times 10^4$ yr are shown in Figure 4. Because of the self-gravitational instability, spiral arms are formed in the density distribution. In the spiral arms, the temperature is also increased because of the compressional heating. The spiral arms are thus seen in the temperature map.

The results of the radiative transfer calculation are shown in Figure 5. The left panels show the brightness temperature images at 1.3 mm, and the right panels show the brightness temperature profile along the major axis shown by the dashed lines in the left panels. The results of the face-on view without beam convolution, the face-on view with convolution, the inclined view without convolution, and the inclined view with convolution, are presented in each row from top to bottom. Spiral structures are seen in the panels without inclination. On the contrary, after the inclination the spiral features are only marginally discernible. In particular, the case of the inclined disk with convolution (the fourth row), which should be the representative of the actual observations, does not clearly exhibit a sign of the spiral structure. These results imply that the effect of the beam convolution and the inclination makes the spiral structure undetectable in the eDisk observations. The apparent absence of spiral features in the eDisk 1.3-mm image in IRAS 16544 thus does not necessarily indicate the real absence of

spiral structures and gravitational instability in the disk.

The intensity profiles along the major axis show hints of the internal structures of the disk. The intensity profile of the face-on, no convolution case presents a number of local emission maxima originated from the spiral features. Whereas these local emission maxima are smoothed out by the effects of the beam convolution and inclination, the intensity profiles in the other three cases still show bumps. In the case of the inclined, convolved case, *i.e.*, observational case, they are seen as an almost symmetric shoulder structure on both side along the major axis.

3.2 Models 2 and 3: High Surface Density Case

The surface density and temperature distributions obtained from the numerical simulation of Model 2, with the initial disk gas mass of 0.17 M_\odot and the surface density 1.75 times higher than that of Model 1, are shown in Figure 6. The model images and intensity profiles along the major axis after the radiative transfer calculations are shown in Figure 7. Similar to Model 1, spiral features are barely seen in the inclined and real observational cases. On the other hand, the flipped intensity profiles along the major axis (black dotted lines in Figure 7 right) reveal an asymmetry. In particular, the real observational case shows an asymmetric shoulder feature (Figure 7 bottom-right).

The surface density and temperature distributions of Model 3 at $t = 3.5 \times 10^3$ yr and $t = 4.1 \times 10^3$ yr are shown in Figures 8 and 9, respectively. This is the case of the most massive disk with the initial disk gas mass of 0.21 M_\odot and the surface density more than twice higher than that of Model 1. The model exhibits a three-arm, $m = 3$ mode feature in the outer part of the disk both in the density and temperature maps at $t = 3.5 \times 10^3$ yr. After $t = 3.9 \times 10^3$ yr the disk fragments into two components. Since the observed disk does not show such a fragment feature, the earlier-time result is adopted for the radiative transfer calculation. The model images and intensity profiles along the major axis after the radiative transfer calculations of Model 3 at $t = 3.5 \times 10^3$ yr are shown in Figure 10. The $m = 3$ pattern creates a clear asymmetric intensity profile along the disk major axis, particularly evident in the non-convolved cases (Figure 10). Even in the inclined and convolved case, the intensity profile along the major axis shows a clear asymmetry, and there is a shoulder feature at $r \sim 15$ au to the righthand side (bottom-right panel of Figure 10).

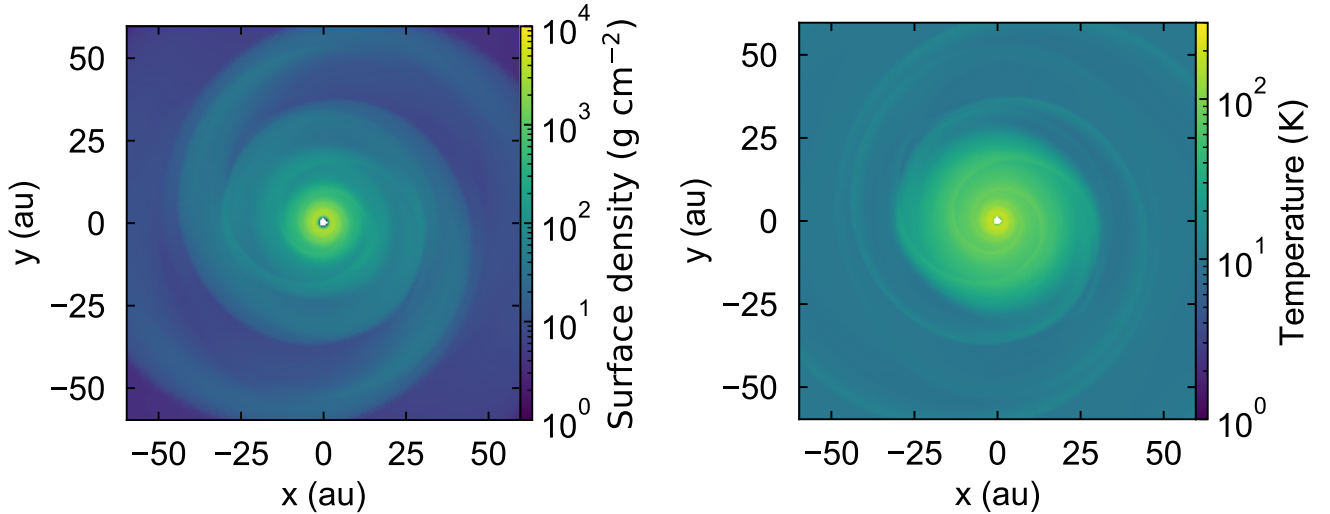


Fig. 4: Results of the numerical simulation of the self-gravitating disk of Model 1 at $t \sim 2.4 \times 10^4$ yr after the start of the simulation. The left and right panels show the surface density and the temperature images, respectively. The white regions at the center of these panels correspond to the inner boundary of the simulation. The spiral structures are formed in both surface density and temperature distributions due to the gravitational instability and the compressional heating. Alt text: Two color images.

Figure 11 compares the observed and Models 1, 2, and 3 intensity profiles along the major axis, where the intensity scales are normalized with the peak intensities for a direct comparison of the profile shapes. All the models reveal a shoulder feature at similar radii to that of the observed shoulder feature. Model 2 further reproduces the observed overall asymmetric shape of the profile with the peak position offset from the origin. The disk of Model 3 appears most extended toward the outer part, while the extent of Model 1 is the smallest. This follows the degree of the gravitational instability, where under a weaker gravitational instability gas tends to accumulate toward the center.

These results imply that spiral arms created by the gravitational instability (GI) could be the source of the shoulder and asymmetric features observed in the protostellar disks.

4 Discussion

4.1 Required Resolution and Sensitivity to Reveal the Spirals

As demonstrated above, the effects of the beam convolution and disk inclination hide the spiral structures created by GI. In the case of the disk in IRAS 16544 with an inclination angle of $\sim 73^\circ$, the projected spatial scale is shrunk by $\sim 30\%$ along the minor axis. It is thus required to investigate the intensity profile along the major axis to study internal structures in the disk. Figure 12 (left) shows the radial profile of the dust optical depth at 1.3 mm along the major axis in Model 1 (inclined view without convolution; the third row of Figure 5). Over almost the entire radius of the observed dust disk ($r_{\text{dust}} = 30$ au), the 1.3-mm dust-continuum emission is optically thick. This implies that the spiral structures seen in the model images reflect the temperature enhancements due to the compressional heating in the spirals. Figure 12 (right) shows the relevant model radial profiles of the brightness and dust temperatures. Note that the brightness temperature profile is affected by the disk inclination while the dust temperature is not. The brightness temperature (blue line) is lower than the dust temperature (orange dashed line), because the brightness temperature of the inclined disk with

a certain thickness is affected by the outer, colder dust located on the front side of the line of sight. In addition, the detailed structure in the dust temperature distribution within $r \sim 10$ au is smoothed out in the brightness temperature distribution because of the inclination effect. Only the substructures at $r \sim 13$ au and ~ 30 au originated from the spirals can be identified in the brightness temperature profile.

The observational beam size should be small enough to resolve these substructures. Here the spiral radius r_{spiral} is defined as the radius of the local maxima of the dust temperature. The minimum dust temperature of the spiral is defined from the intensity of the local minima closest to the local maxima, and the spatial coverage above that local minima is defined as the width of the spirals Δ . Figure 13 shows the radial distribution of Δ normalized over the spiral radius r_{spiral} . Δ is $\lesssim 0.1r$ in half of the data points. In addition, Δ is similar to the pressure scale height (dashed line in Figure 13), which is a typical length scale of the self-gravitational instability. Figure 14 shows the radial distribution of Δ normalized by the beam size of the eDisk observations of ~ 4.5 au. In all the spirals over the dust disk radius of 30 au, Δ is smaller than the beam size. To unveil the spiral structure Δ should be sampled at least three independent beams, implying that the a factor $\gtrsim 10$ finer beam size of $\lesssim 0.5$ au is required.

To investigate the effect of the direction of the azimuthal cuts, Figure 15 shows the inclined, beam-convolved images and intensity profiles of Model 1 for different azimuthal directions of the disk major axes. Depending on the azimuthal directions, a spiral feature in the outer part of the disk appears in the 1 and 3σ contours, but not in the 5σ contour. Thus, $\gtrsim 2$ times longer observing time is also required to detect the outer spirals. Note that symmetric shoulder-like structures are evident in the right panels of Figure 15 and their radii vary depending on the observing direction. This result implies that the position of the shoulder structure formed by the spirals depends on the observation timing of the orbital motion.

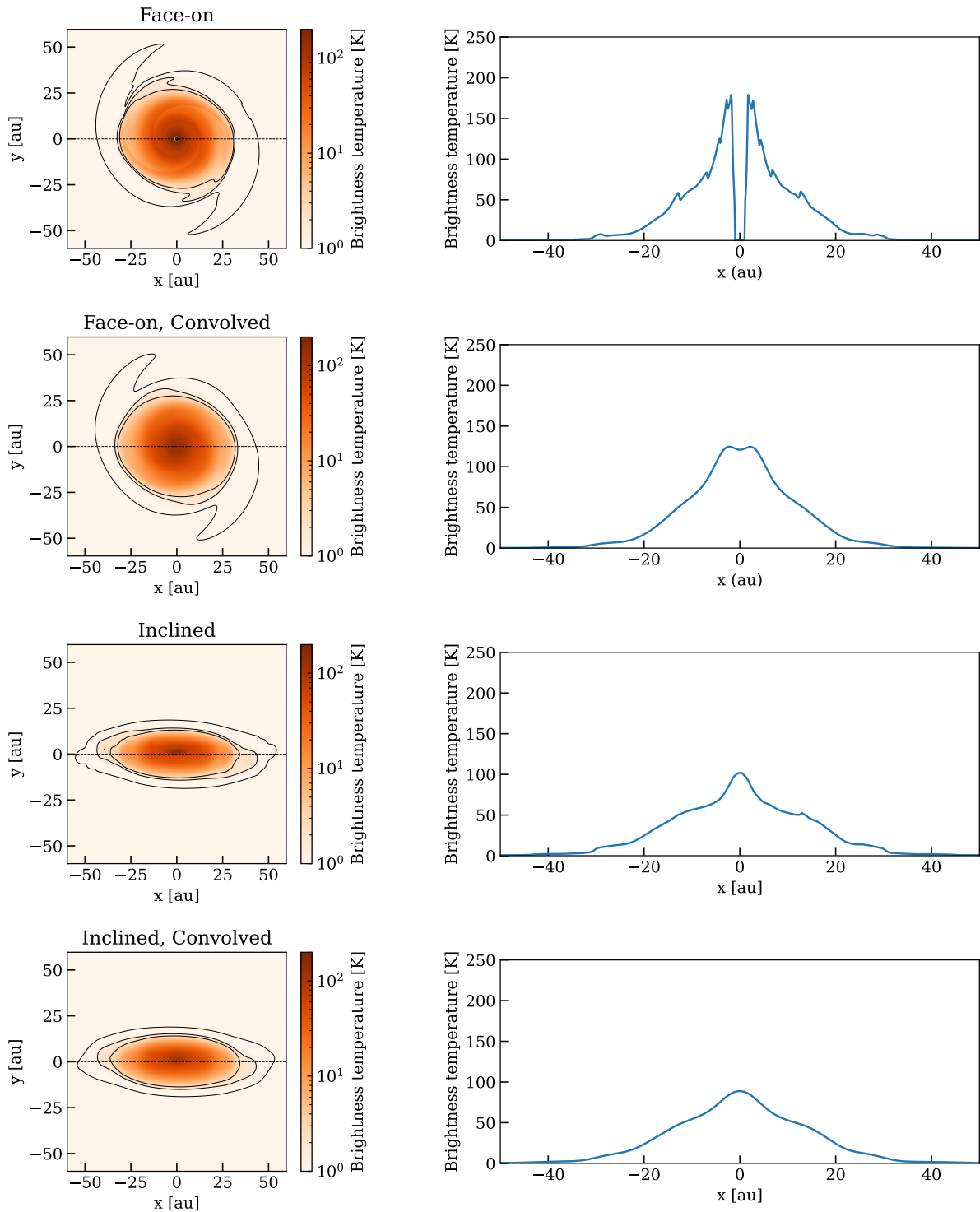


Fig. 5: 1.3-mm dust continuum images (left) and intensity profiles along the major axis of the model disk (right) obtained with the radiative transfer calculations. Contour levels in left panels are 1σ , 3σ , and 5σ of the eDisk observations ($1\sigma = 0.5$ K). The corresponding density and temperature distributions are shown in Figure 4. Dashed lines denote the cuts of the intensity profile of the relevant right panels. The results of the face-on view without beam convolution, the face-on view with convolution, the inclined view without convolution, and the inclined view with convolution, are presented in each row from top to bottom. In the panels of the face-on view without convolution (the first row), the brightness temperature is decreased in the central region because of the inner boundary of the simulation. Alt text: Four color and contour images in the left column, and four line graphs in the right column. In the right column, x axis shows the positional offset from the protostellar position from -50 to 50 astronomical unit. The y axis shows the brightness temperature from 0 Kelvin to 250 Kelvin.

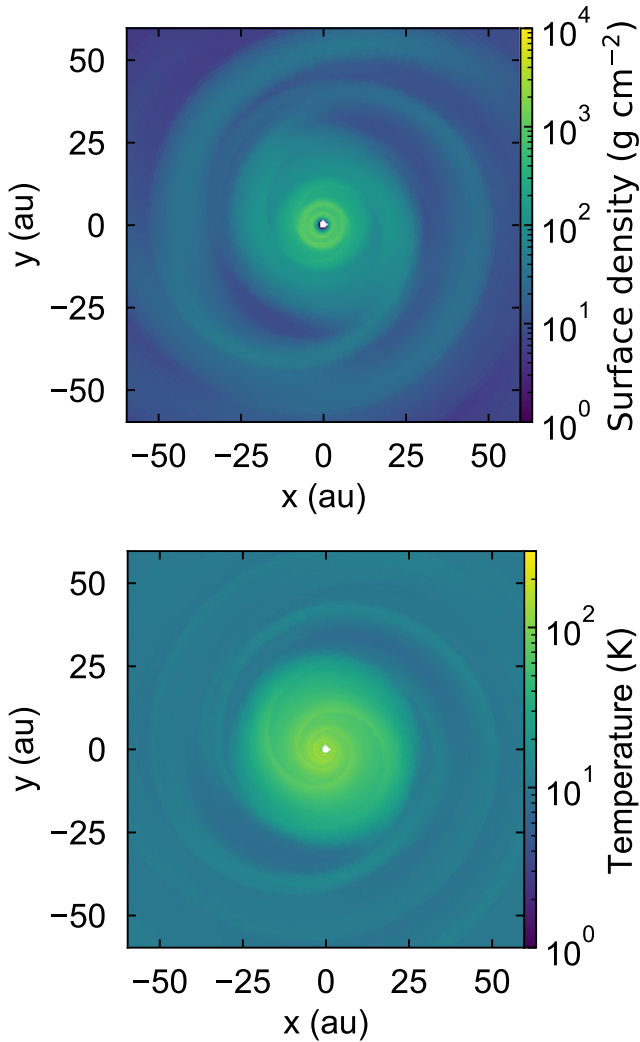


Fig. 6: Same as Figure 4 but for Model 2. Alt text: Two color images.

4.2 Flared Dust Distribution in Young Protostellar Disks

Our 2-dimensional simulations and radiative transfer calculations assume that dust grains of all sizes are flared following eqs. 9 and 10. Our modeling thus does not consider the difference of the scale height depending on the dust sizes. The use of Rosseland mean opacity to calculate the dust temperature in the 2-dimensional FARGO-ADSG simulations implicitly assumes the vertically uniform dust distribution regardless of the dust size. The 1.3-mm dust-continuum emission is sensitive to sub-millimeter-size dust grains, which are considered to be more settled onto the disk midplane than smaller grains, as in the case of protoplanetary disks with ring and gap features (e.g., Pinte et al. 2016; Villenave et al. 2022). If such dust settling is present in IRAS 16544, our simulations and radiative transfer calculations could over-estimate the observability of the spiral features.

Our eDisk observations of young protostellar disks, however, show that large dust grains traced by the 1.3-mm continuum emission are likely flared. Several of eDisk targets, including IRAS 16544, exhibit asymmetric intensity profiles along the disk minor axes. Our radiative transfer modeling demonstrates that such asymmetric intensity profiles can be interpreted as the flaring of large dust and the optically-thick dust-continuum emission

(Takakuwa et al. 2024). Furthermore, in gravitationally unstable disks, turbulent viscosity

$$\nu_{\text{vis}} = \alpha c_s H \quad (11)$$

is considered to be high because of a large effective viscous parameter α (≥ 0.01) inferred from hydrodynamic simulations (e.g., Gammie 2001; Rice et al. 2005). Such a high turbulent α is sufficient to maintain a high scale height of sub-mm-sized dust grains. Therefore, in the case of younger, protostellar disks, flared distribution of sub-mm-sized dust grains is expected and the present 2-dimensional FARGO-ADSG simulations along with the radiative transfer calculations should be valid to discuss the observability of the internal spiral features.

4.3 Implications for Formation and Evolution of Disk Internal Structures

Our numerical simulations along with the radiative transfer calculations demonstrate that a shoulder feature can be reproduced by spiral arms in a marginally gravitationally unstable ($Q \sim 2$) disk model (Model 1). In a more massive, gravitational unstable disk (Model 2; $Q \sim 1.3$), an asymmetric feature along the disk major axis can also be created. In the disk more massive than the central protostar (Model 3; $Q \sim 1$), a three-arm, $m = 3$ mode can also be produced, which exhibits a clear asymmetric shoulder feature in the intensity profile along the major axis.

Similar asymmetric bump features are seen toward Ced110 IRS4A, and intriguing western, central, and eastern peaks are seen in the disk toward Ced110 IRS4B (Sai et al. 2023). In L1527 IRS, the southern part of the disk is clearly stronger than the northern part (van't Hoff et al. 2023). Class 0 sources of IRAS 16253-2429 (Aso et al. 2023), R CrA IRS5N (Sharma et al. 2023), and a Class I source R CrA IRS7B-a (Takakuwa et al. 2024), show the skewed intensity peaks along the disk major axes. Except for R CrA IRS7B-a, sources with such disk substructures are all Class 0 sources associated with Keplerian rotations. In the case of an even younger source of B335, a clear disk like signature in the 1.3-mm dust-continuum emission and the Keplerian rotation are not identified (Yen et al. 2015; Ohashi et al. 2023). On the other hand, most evolved Class I sources in our eDisk sample, L1489 IRS and Opt IRS63, exhibit ring-gap features, while the image contrasts between the rings and gaps are not as evident as those in the Class II sources. These results suggest that the shoulder, bump, and/or asymmetric peaks may be common features in the Class 0 disks.

Our results indicate that these observations do not conflict with previous theoretical studies of disk formation and evolution processes, which show that young disks are massive enough to be gravitationally unstable and to form spiral arms (Inutsuka et al. 2010; Zhao et al. 2018; Tsukamoto et al. 2020). This is also important to understand formation mechanism of ring-gap structures observed in more evolved disks than those observed by eDisk. One of the commonly accepted mechanisms of ring-gap formation is the carving by the hidden planet (Paardekooper et al. 2023). The observed gap radii, however, reaches ~ 100 au (Bae et al. 2023), where it is difficult to form the planet by the core accretion within the timescale of the disk age ($\lesssim 10^6$ yr). Thus, gravitational fragmentation of the disk (Boss 1997) is one of the possible mechanisms to form the gap-forming planet because the timescale of the gravitational collapse is comparable to the dynamical timescale of the disk (Booth & Ilee 2020). The disk self-gravity can also produce ring-gap structures without hidden planets. Previous study indicates that ring-gap structures can be formed by the secular gravitational instability (Takahashi & Inutsuka 2014, 2016; Tominaga

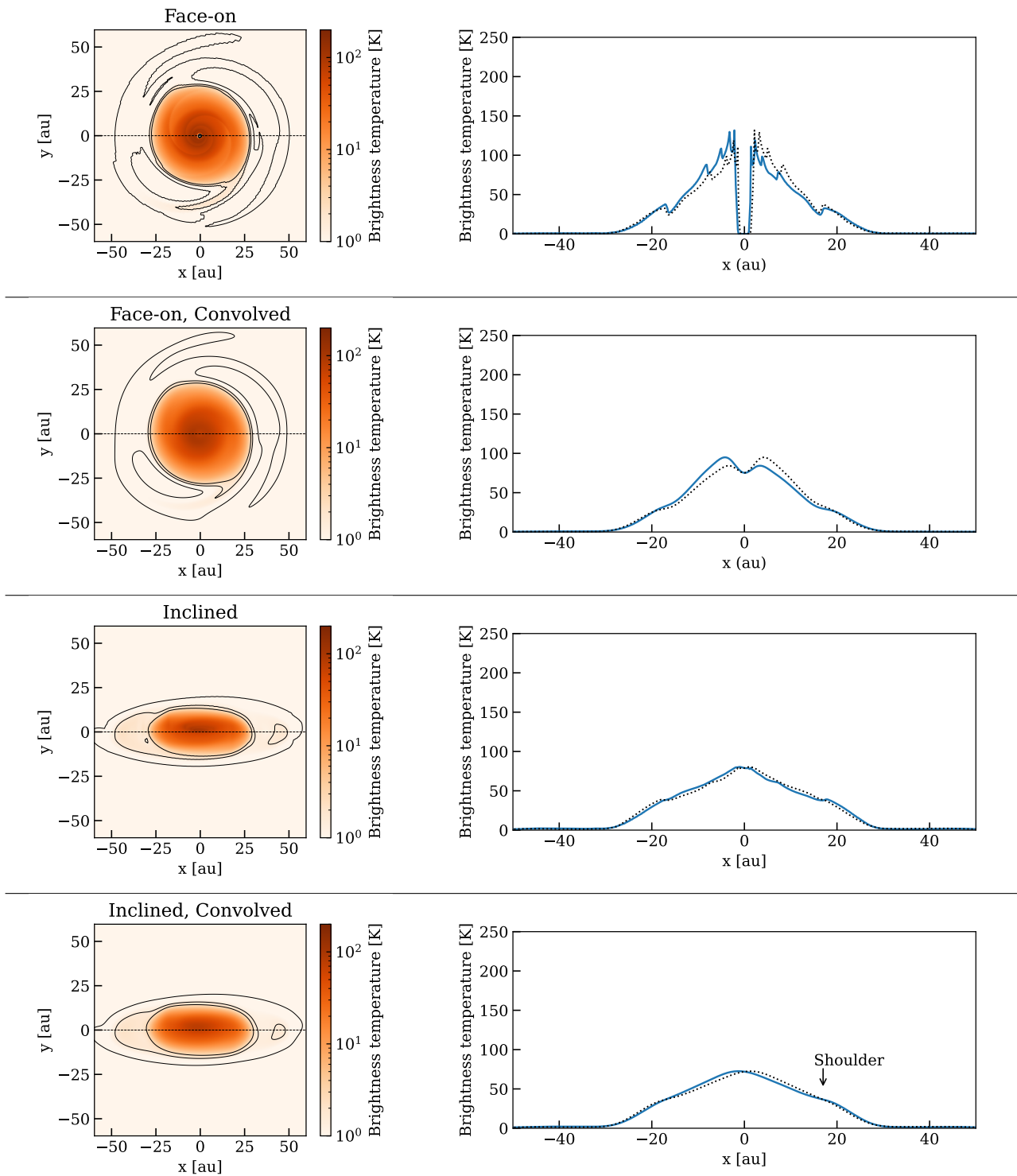


Fig. 7: Same as Figure 5 but for Model 2. Dotted lines in the left panels denote the intensity profile flipped horizontally, to show the asymmetry of the intensity profiles more clearly. A possible shoulder structure to the right hand side of the intensity profile is seen in the inclined and convolved case. Alt text: Four color and contour images in the left column, and four line graphs in the right column. In the right column, x axis shows the positional offset from the protostellar position from -50 to 50 astronomical unit. The y axis shows the brightness temperature from 0 Kelvin to 250 Kelvin.

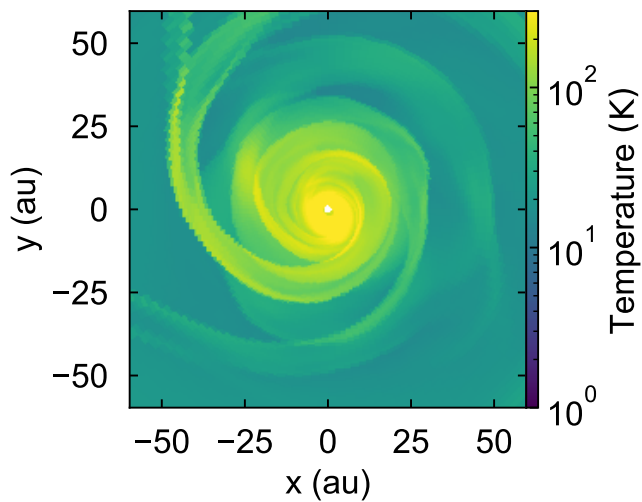
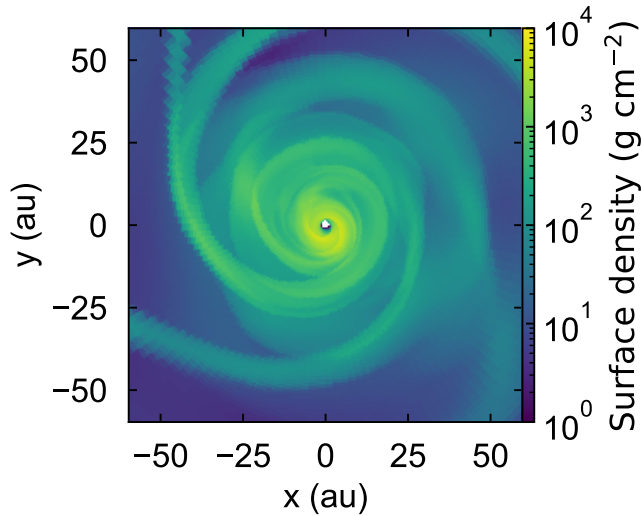


Fig. 8: Same as Figure 4 but for Model 3 at $t = 3.5 \times 10^3$ yr after the start of the simulation. Alt text: Two color images.

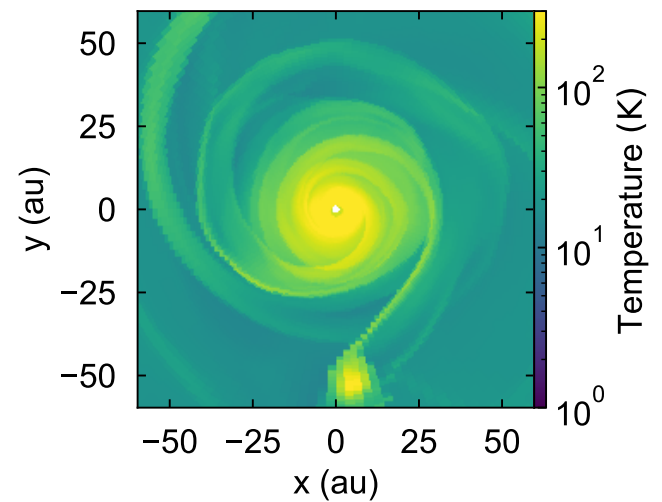
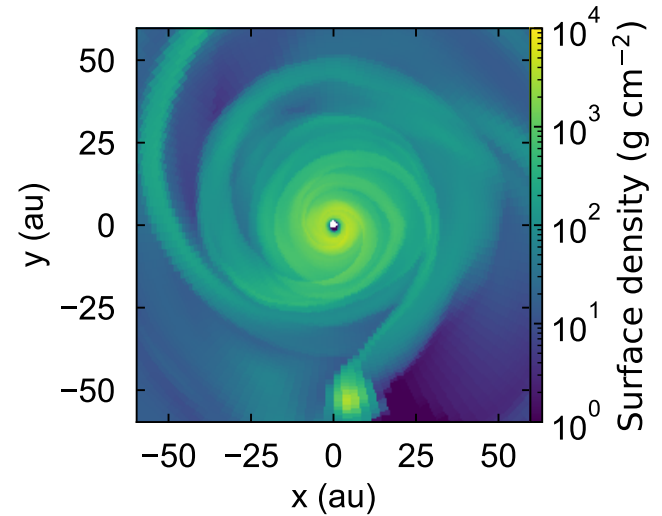


Fig. 9: Same as Figure 4 but for Model 3 at $t = 4.1 \times 10^3$ yr after the start of the simulation. Alt text: Two color images.

et al. 2018, 2020). While this instability can grow even if the disk is gravitationally stable, self-gravity can further facilitate this instability. Thus, the prevalence of the ring-gap feature in evolved disks favors gravitational instability in protostellar disks. Because the mass infall rate from the envelope onto the disk decreases with time and the disk gas accretes onto the central star, the disk surface density will decrease with time evolution. Thus, more evolved disks such as those observed by DSHARP are expected to be gravitationally stable even if the disks are gravitationally unstable in their protostellar disk stage.

At present, however, our study is a case-study of only one eDisk target, IRAS 16544. In this particular case, the spiral arms due to gravitational instability, if present, cannot be imaged due to the effect of the beam size and the inclination. Further modeling and radiative transfer calculations of a statistically significant sample of protostars are required to discuss physical conditions and evolution of protostellar disks into planet formation.

5 Conclusions

We constructed numerical models of self-gravitating protostellar disks and performed radiative transfer calculations of the physical models. The model images exhibit spiral structures caused by the gravitational instabilities. We made detailed comparisons of those model images to the 1.3-mm image of the protostellar disk around the Class 0 protostar IRAS 16544 observed with eDisk. The effects of the disk inclination and the observational spatial resolution are incorporated, and the origin of the shoulder feature as well as the apparent absence of the spiral features in the eDisk image is discussed. The findings of this work are summarized as follows:

- Spiral structures formed by the gravitational instability in the model disks are undetectable in the images after the effects of the inclination and beam convolution are incorporated. This indicates that the non-detection of a clear spiral structure in the disk image around IRAS 16544 does not reject the presence of gravitational instability and spiral features. Since a young disk is expected to be gravitationally unstable by many, although not all, numerical studies of disk formation and evolution, this result shows that the observations are not inconsistent with previous understandings of protostellar disk evolution.

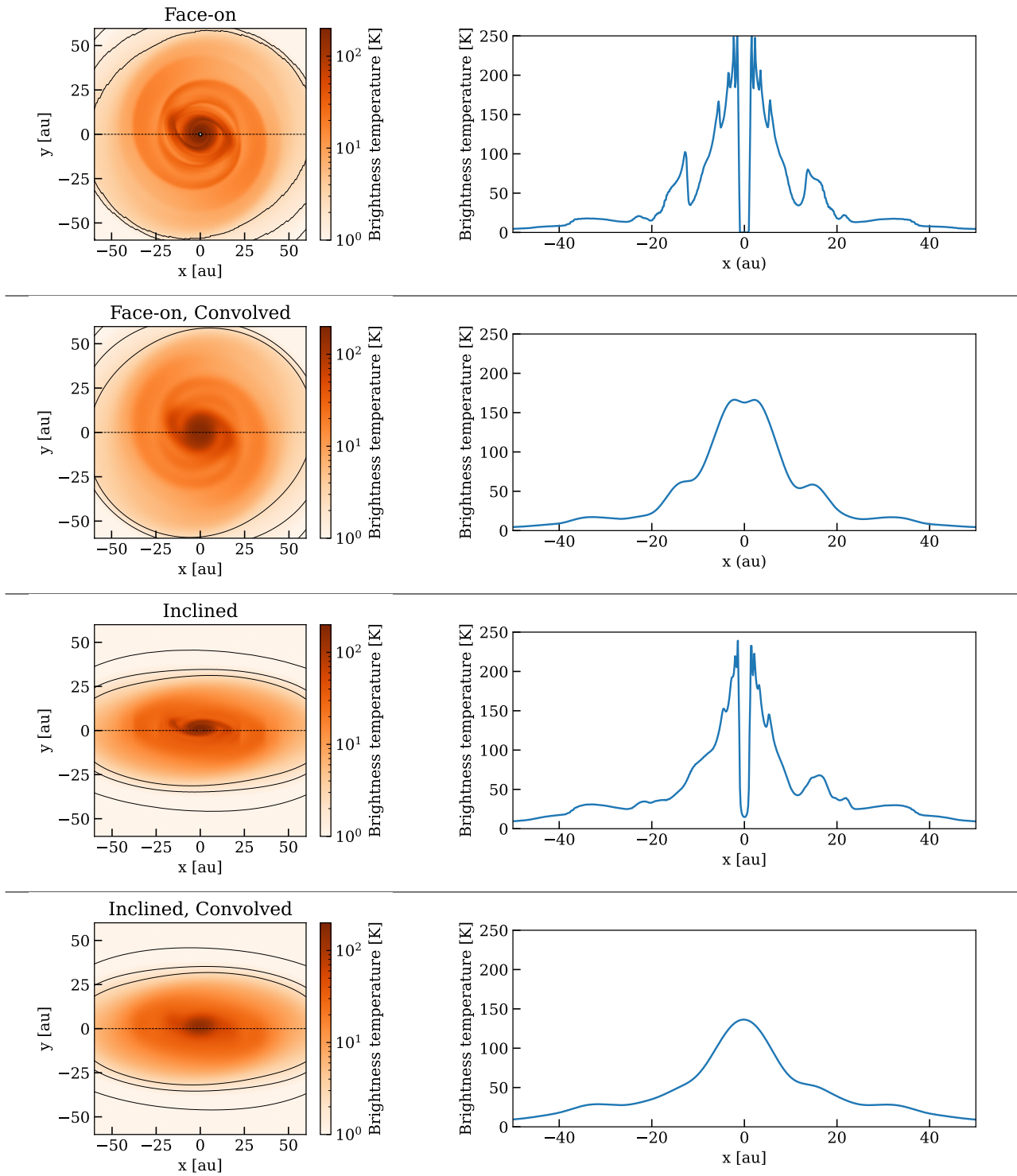


Fig. 10: Same as Figure 5 but for Model 3 at $t = 3.5 \times 10^3$ yr. Alt text: Four color and contour images in the left column, and four line graphs in the right column. In the right column, x axis shows the positional offset from the protostellar position from -50 to 50 astronomical unit. The y axis shows the brightness temperature from 0 Kelvin to 250 Kelvin.

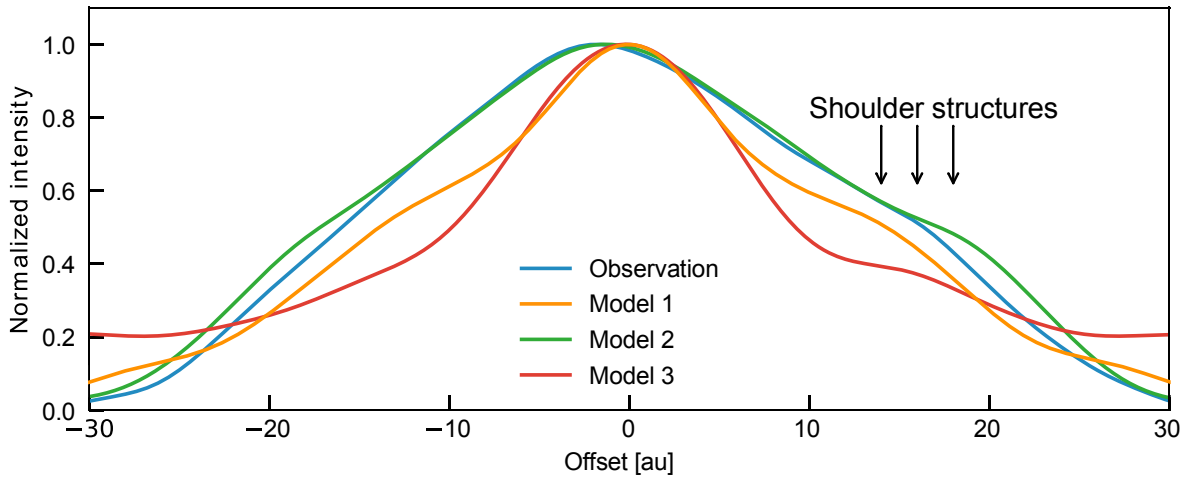


Fig. 11: Normalized intensity profiles along the major axis in the observations (blue), Model 1 (orange), Model 2 (green), and **Model 3** (red). Horizontal axis shows the offset from the center, where the positive offset corresponds to the side with the shoulder structure. Alt text: Line graph. x axis shows the positional offset from the protostellar position from -30 to 30 astronomical unit. The y axis shows the normalized intensity from 0 to 1.1.

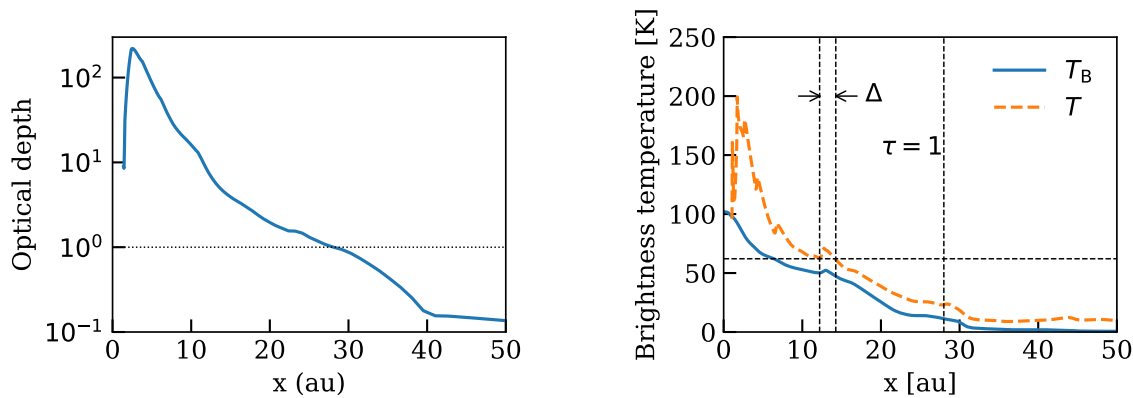


Fig. 12: Radial profile of the optical depth at 1.3 mm (left panel) and that of the 1.3-mm brightness temperature and the dust temperature of the disk model (right panel) along the major axis of Model 1. The rapid decrease of the profiles around the center is the artifact of the inner boundary of the numerical simulation. In the right panel, the brightness temperature and the dust temperature are shown by solid blue and dashed orange lines, respectively. The width of the spiral Δ is defined by the spiral region where the temperature is higher than the closest local minima (see the horizontal dashed line). The vertical dashed line at $x = 28$ au shows the radius where $\tau = 1$. Alt text: Two line graphs. x axis shows the radius from 0 to 50 astronomical unit.

- Because the 1.3-mm dust-continuum emission in the model disk is optically thick over an almost entire extent of the dust disk ($r \lesssim 30$ au), the intensity profile traces the temperature distribution. The width of the spiral structure in the temperature distribution is measured, and the required beam size to resolve the spiral structure is as small as ~ 0.5 au in the inner ($\lesssim 15$ au) radii, which is ~ 10 times finer than that of the eDisk observations. In the outer radii, \sim twice longer observing time is required to clearly image the spiral structure.
- The 1.3-mm eDisk image of the protostellar disk in IRAS 16544 shows an asymmetric shoulder structure in the intensity profile along the major axis. We found that the asymmetric shoulder-like structure can be reproduced when the disk is massive enough ($Q \lesssim 1.3$). In the model disk more massive than the central protostar, a three-arm, $m = 3$ mode is also formed, which exhibits a clear asymmetric shoulder structure in

the intensity profile along the disk major axis. Shoulder-like or bump features are also observed in other eDisk samples, mostly Class 0 sources. Those observational results may suggest self-gravitating disks around those protostars in the early stage of disk evolution, before the stage of gap and ring features caused by the protoplanets.

ACKNOWLEDGEMENTS

This paper makes use of the following ALMA data: ADS/JAO.ALMA #2019.1.00261.L and 2019.A.00034.S. ALMA is a partnership of ESO (representing its member states), NSF (USA), and NINS (Japan), together with NRC (Canada), NSTC and ASIAA (Taiwan), and KASI (Republic of Korea), in cooperation with the Republic of Chile. The Joint ALMA Observatory is operated by ESO, AUI/NRAO, and NAOJ.

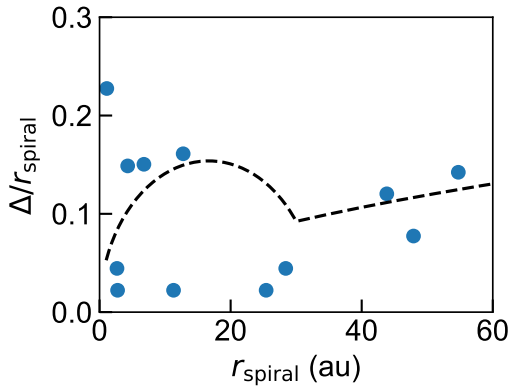


Fig. 13: Radial distribution of the spiral width Δ normalized by the radius of the spiral r_{spiral} calculated from the dust temperature profile along the major axis (the right panel of Figure 12). The dashed line shows the pressure scale height normalized by the radius calculated from Equation 9, where the temperature profiles given in Equation 7 is adopted. Alt text: Line graph and plot of the data points. x axis shows the radius from 0 to 60 astronomical unit. y axis shows the normalized radius of the spiral location from 0 to 0.3.

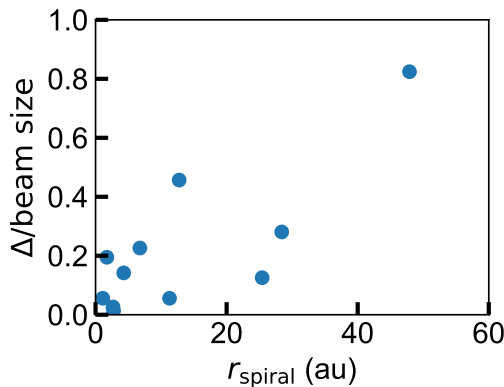


Fig. 14: Radial distribution of the width of the spiral Δ normalized by the beam size of the IRAS 16544 observations. Alt text: Plot of the data points. x axis shows the radius from 0 to 60 astronomical unit. y axis shows the normalized spiral width from 0 to 1.

Numerical computations and analyses were in part carried out on Small Parallel Computers and analysis servers at Center for Computational Astrophysics, National Astronomical Observatory of Japan. S.T. is supported by JSPS KAKENHI grant Nos. JP21H00048, JP21H04495, and JP24K00674, and by NAOJ ALMA Scientific Research grant No. 2022-20A. K.S. is supported by JSPS KAKENHI grant No. JP21H04495 and by NAOJ ALMA Scientific Research grant No. 2022-20A.

Appendix A: Radiative Transfer Modeling of the Dust Disk of IRAS 16544-1604

To investigate the effect of the flared disk structure on the determination of the central protostellar position and the major and minor axes through the 2-dimensional Gaussian fitting, radiative transfer calculations with RADMC3d have been conducted. The physical model of the protostellar disk and envelope is the same as that described by Takakuwa et al. (2024), *i.e.*, a Keplerian disk with a vertically hydrostatic equilibrium plus a rotating and in-falling envelope taken from Ulrich (1976); Hartmann et al. (1994); Mendoza et al. (2004). Several of the model parameters are tailored to the case of IRAS 16544 (Table 2), where the protostellar and disk mass, and the gas and dust disk radii are identical to those of Model 1 in our FARGO-ADSG modeling. Search for the other parameters was made to approximately match the observed and model images after the convolution with the observed beam. Other model parameters not listed in Table 2 are the same as those of the fiducial model in Takakuwa et al. (2024). As the purpose of the present radiative transfer calculations is to investigate the effect of the flared disk structure on the determination of the central protostellar position and the major and minor axes, further fine tuning of the model parameters to have an even better match of the model image with the observed image, as well as interferometric observing simulations, is not performed.

Figure 16 shows the observed and model images as well as the residual images after the fitting of the 2-dimensional Gaussian fitting. The protostellar position of the model image is set to be the centroid position as derived from the 2-dimensional Gaussian fitting to the observed image ($16^{\text{h}}57^{\text{m}}19.6428^{\text{s}}$, $-16^{\circ}09'24''.016$; white crosses in Figure 16). The 2-dimensional Gaussian fitting to the model image gives the Gaussian centroid position of ($16^{\text{h}}57^{\text{m}}19.6427^{\text{s}}$, $-16^{\circ}09'24''.015$), which is indistinguishable from the central protostellar position. The position angle as derived from the 2-dimensional Gaussian fitting is $45.3^{\circ} \pm 1.1^{\circ}$, same as that of the correct answer of 45° . We thus consider that the effect of the flared disk structure is not significant for the determination of the disk center and the major and minor axes through the 2-dimensional Gaussian fitting.

Both the observed and model residual images show a positive, horseshoe feature to the northwest. This asymmetric pattern in the residual images reflects the asymmetric intensity profiles along the disk minor axis due to the flared disk geometry (Takakuwa et al. 2024). Negative patterns to the northwest and southeast, and residual peaks around the protostellar position, are also seen, which show deviation of the intensity profile from the Gaussian profile.

Software: CASA (McMullin et al. 2007), matplotlib (Hunter 2007), APLpy (Robitaille & Bressert 2012; Robitaille 2019), astropy (Astropy Collaboration et al. 2022), FARGO-ADSG (Masset 2000; Baruteau 2008; Baruteau & Masset 2008).

Facility: ALMA.

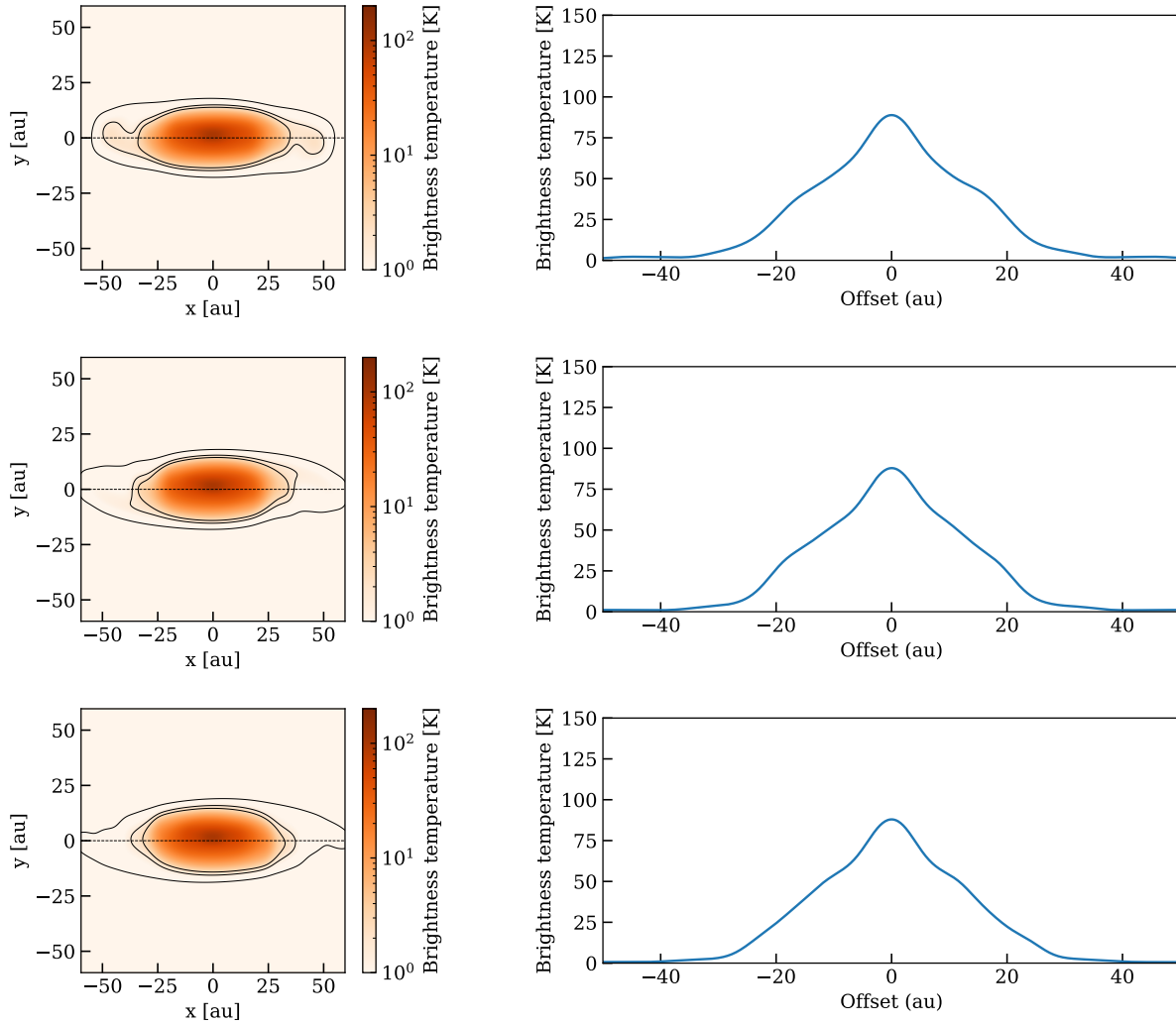


Fig. 15: Inclined and beam-convolved model images (left panels) and intensity profiles along the major axis (right) with a different azimuthal angle of the disk major axes. These correspond to the bottom panels of Figure 5 but the azimuth angle is rotated by 45° , 90° , and 135° proceeding from top to bottom. The contour levels in left panels are 1σ , 3σ , and 5σ of the eDisk observations ($1\sigma = 0.5$ K). Alt text: Three color and contour images in the left column, and three line graphs in the right column. In the right column, x axis shows the positional offset from the protostellar position from -50 to 50 astronomical unit. The y axis shows the brightness temperature from 0 Kelvin to 150 Kelvin.

Table 2: Parameters of the radiative transfer modeling.

Protostellar mass	$0.14 M_\odot$
Protostellar luminosity	$0.89 L_\odot$
Gas disk mass	$0.1 M_\odot$
Gas disk radius	60 [au]
Dust disk radius	30 [au]
Inclination angle	-73°
Position Angle	45°
Disk flaring index p ($H \sim r^p$)	1.0
Mass infalling rate	$2.0 \times 10^{-6} M_\odot \text{ yr}^{-1}$
Number of photons	100000

References

- ALMA Partnership, Brogan, C. L., Pérez, L. M., et al. 2015, ApJL, 808, L3,
 Andrews, S. M., Wilner, D. J., Zhu, Z., et al. 2016, ApJL, 820, L40,
 Andrews, S. M., Huang, J., Pérez, L. M., et al. 2018, ApJL, 869, L41,
 Aso, Y., Kwon, W., Ohashi, N., et al. 2023, ApJ, 954, 101,
 Astropy Collaboration, Price-Whelan, A. M., Lim, P. L., et al. 2022, ApJ, 935, 167,
 Bae, J., Isella, A., Zhu, Z., et al. 2023, in Astronomical Society of the Pacific Conference Series, Vol. 534, Protostars and Planets VII, ed. S. Inutsuka, Y. Aikawa, T. Muto, K. Tomida, & M. Tamura, 423,
 Baruteau, C. 2008, PhD thesis, CEA Saclay, Service d’Astrophysique, 91191

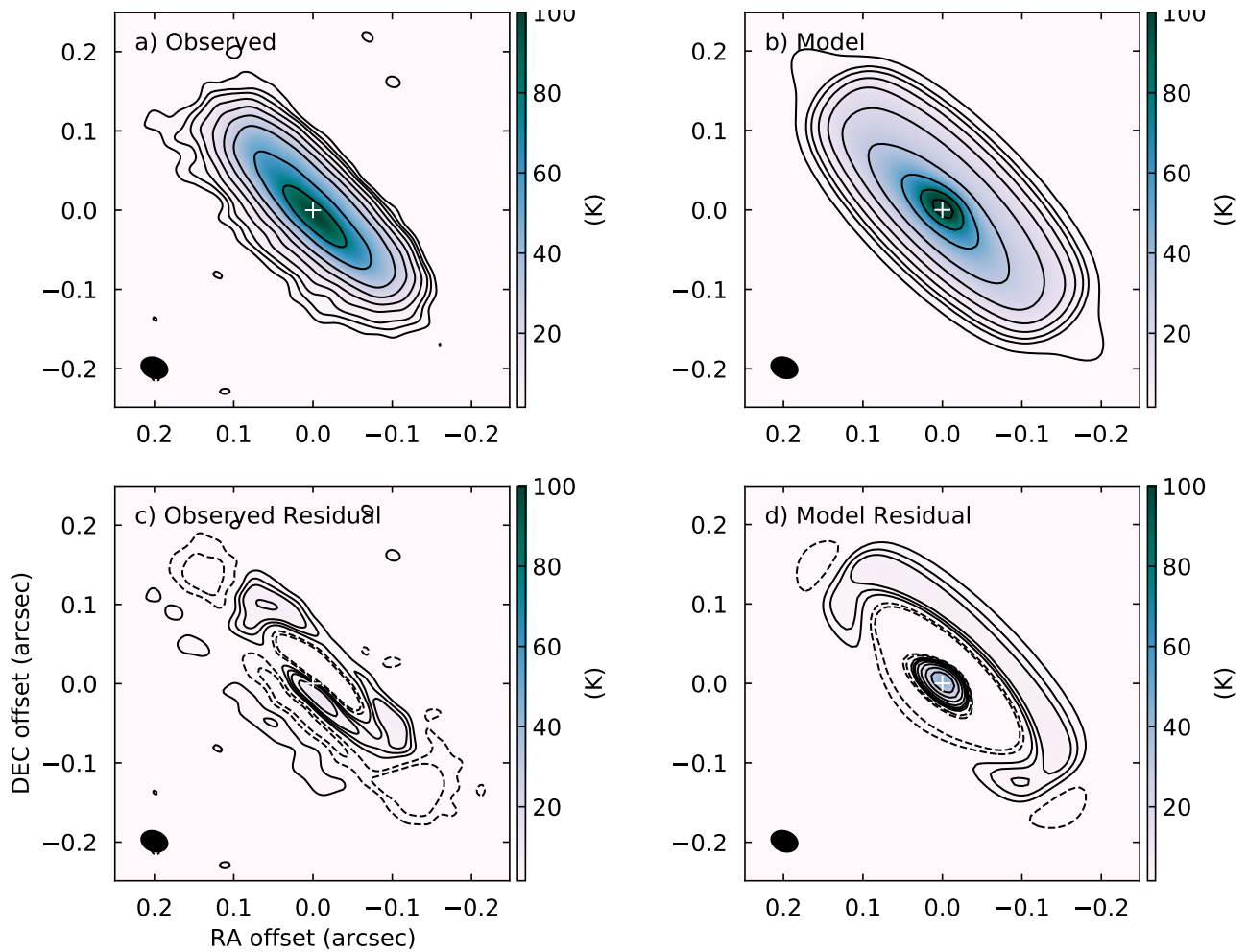


Fig. 16: Observed (a) and model images (b) of the 1.3-mm dust-continuum emission of IRAS 16544, and the residual observed (c) and model images (d) after the 2-dimensional Gaussian fitting. Contour levels are $-\sigma$, -3σ , 3σ , 6σ , 9σ , 15σ , 25σ , 40σ , 60σ , 100σ , 150σ , 200σ ($1\sigma = 0.522$ K). Filled ellipses at the bottom-left corners denote the beam size ($0''.0364 \times 0''.0275$; P.A. = 69.5°). Alt text: Four color and contour images.

Gif/Yvette Cedex, France

Baruteau, C., & Masset, F. 2008, *ApJ*, 678, 483,

Bate, M. R. 1998, *ApJL*, 508, L95,

Bertin, G., & Lodato, G. 1999, *A&A*, 350, 694

Birnstiel, T., Dullemond, C. P., Zhu, Z., et al. 2018, *ApJL*, 869, L45,

Booth, A. S., & Ilee, J. D. 2020, *MNRAS*, 493, L108,

Boss, A. P. 1997, *Science*, 276, 1836,

Dullemond, C. P., Juhasz, A., Pohl, A., et al. 2012, RADMC-3D: A multi-purpose radiative transfer tool, *Astrophysics Source Code Library*, record ascl:1202.015.

Fedele, D., Carney, M., Hogerheijde, M. R., et al. 2017, *A&A*, 600, A72,

Fedele, D., Tazzari, M., Booth, R., et al. 2018, *A&A*, 610, A24,

Flores, C., Ohashi, N., Tobin, J. J., et al. 2023, *ApJ*, 958, 98,

Fukagawa, M., Tsukagoshi, T., Momose, M., et al. 2013, *PASJ*, 65, L14,

Gammie, C. F. 2001, *ApJ*, 553, 174,

Hartmann, L., Boss, A., Calvet, N., & Whitney, B. 1994, *ApJL*, 430, L49,

Hubeny, I. 1990, *ApJ*, 351, 632,

Hunter, J. D. 2007, *Computing in Science and Engineering*, 9, 90,

Inutsuka, S., Machida, M. N., & Matsumoto, T. 2010, *ApJL*, 718, L58,

Isella, A., Guidi, G., Testi, L., et al. 2016, *Physical Review Letters*, 117, 251101,

Kido, M., Takakuwa, S., Saigo, K., et al. 2023, *ApJ*, 953, 190,

Kornet, K., Bodenheimer, P., Różyczka, M., & Stepinski, T. F. 2005, *A&A*, 430, 1133,

Machida, M. N., Inutsuka, S., & Matsumoto, T. 2011, *PASJ*, 63, 555.

Masset, F. 2000, *A&AS*, 141, 165,

McMullin, J. P., Waters, B., Schiebel, D., Young, W., & Golap, K. 2007, in *Astronomical Society of the Pacific Conference Series*, Vol. 376, *Astronomical Data Analysis Software and Systems XVI*, ed. R. A. Shaw, F. Hill, & D. J. Bell, 127

Mendoza, S., Cantó, J., & Raga, A. C. 2004, *Rev.Mex.Astron.Astrofis.*, 40, 147,

Mordasini, C., Alibert, Y., Benz, W., Klahr, H., & Henning, T. 2012, *A&A*, 541, A97,

Mulders, G. D., Pascucci, I., & Apai, D. 2015a, *ApJ*, 814, 130,

— 2015b, *ApJ*, 798, 112,

Narang, M., Manoj, P., Furlan, E., et al. 2018, *AJ*, 156, 221,

Ohashi, N., Tobin, J. J., Jørgensen, J. K., et al. 2023, *ApJ*, 951, 8,

Paardekooper, S., Dong, R., Duffell, P., et al. 2023, in *Astronomical Society of the Pacific Conference Series*, Vol. 534, *Astronomical Society of the Pacific Conference Series*, ed. S. Inutsuka, Y. Aikawa, T. Muto, K. Tomida, & M. Tamura, 685

Pérez, L. M., Carpenter, J. M., Andrews, S. M., et al. 2016, *Science*, 353, 1519,

- Pinte, C., Dent, W. R. F., Ménard, F., et al. 2016, *ApJ*, 816, 25,
- Rice, W. K. M., Lodato, G., & Armitage, P. J. 2005, *MNRAS*, 364, L56,
- Robitaille, T. 2019, *APLpy v2.0: The Astronomical Plotting Library in Python, 2.0*, Zenodo,
- Robitaille, T., & Bressert, E. 2012, *APLpy: Astronomical Plotting Library in Python, Astrophysics Source Code Library, record ascl:1208.017*
- Sai, J., Yen, H.-W., Ohashi, N., et al. 2023, *ApJ*, 954, 67,
- Santamaría-Miranda, A., de Gregorio-Monsalvo, I., Ohashi, N., et al. 2024, *A&A*, 690, A46,
- Sharma, R., Jørgensen, J. K., Gavino, S., et al. 2023, *ApJ*, 954, 69,
- Sheehan, P. D., & Eisner, J. A. 2017, *ApJL*, 840, L12,
- Sheehan, P. D., Tobin, J. J., Li, Z.-Y., et al. 2022, *ApJ*, 934, 95,
- Takahashi, S. Z., & Inutsuka, S. 2014, *ApJ*, 794, 55,
- . 2016, *AJ*, 152, 184,
- Takakuwa, S., Saigo, K., Kido, M., et al. 2024, *ApJ*, 964, 24,
- Tomida, K., Machida, M. N., Hosokawa, T., Sakurai, Y., & Lin, C. H. 2017, *ApJL*, 835, L11,
- Tominaga, R. T., Inutsuka, S.-i., & Takahashi, S. Z. 2018, *PASJ*, 70, 3,
- Tominaga, R. T., Takahashi, S. Z., & Inutsuka, S.-i. 2020, *ApJ*, 900, 182,
- Toomre, A. 1964, *ApJ*, 139, 1217,
- Tsukamoto, Y., Iwasaki, K., Okuzumi, S., Machida, M. N., & Inutsuka, S. 2015a, *MNRAS*, 452, 278,
- Tsukamoto, Y., Machida, M. N., & Inutsuka, S.-i. 2023, *PASJ*, 75, 835,
- Tsukamoto, Y., Machida, M. N., Susa, H., Nomura, H., & Inutsuka, S. 2020, *ApJ*, 896, 158,
- Tsukamoto, Y., Takahashi, S. Z., Machida, M. N., & Inutsuka, S. 2015b, *MNRAS*, 446, 1175,
- Ulrich, R. K. 1976, *ApJ*, 210, 377,
- van der Marel, N., van Dishoeck, E. F., Bruderer, S., et al. 2013, *Science*, 340, 1199,
- van't Hoff, M. L. R., Tobin, J. J., Li, Z.-Y., et al. 2023, *ApJ*, 951, 10,
- Villenave, M., Stapelfeldt, K. R., Duchêne, G., et al. 2022, *ApJ*, 930, 11,
- Yen, H.-W., Takakuwa, S., Koch, P. M., et al. 2015, *ApJ*, 812, 129,
- Zhao, B., Caselli, P., Li, Z.-Y., & Krasnopolsky, R. 2018, *MNRAS*, 473, 4868,
- Zucker, C., Speagle, J. S., Schlafly, E. F., et al. 2020, *A&A*, 633, A51,